

Algorithms for Poisson Phase Retrieval

Zongyu Li *Student Member, IEEE*, Kenneth Lange and Jeffrey A. Fessler *Fellow, IEEE*

Abstract—This paper discusses algorithms for phase retrieval where the measurements follow independent Poisson distributions, using maximum likelihood (ML) estimation. To optimize the log-likelihood for the Poisson phase retrieval model, we developed and compared several algorithms including Wirtinger flow (WF), Gerchberg Saxton (GS), majorize minimize (MM) and alternating direction method of multipliers (ADMM). Simulation results using random Gaussian sensing matrix and discrete Fourier transform (DFT) matrix under Poisson measurement noise demonstrated that algorithms based on the Poisson model consistently produced higher quality reconstructions than algorithms (WF, GS) derived from Gaussian noise models when applied to such data. Moreover, the reconstruction quality can be further improved by adding regularizers that exploit assumed properties of the latent signal/image, such as sparsity of finite differences (anisotropic total variation) or of the coefficients of a discrete wavelet transform. The proposed regularized MM algorithm decreased NRMSE much faster than the regularized ADMM algorithm. We also proposed a variation of the WF approach that uses a step size based on the Fisher information and converges faster than previous WF approaches.

Index Terms—Poisson Phase retrieval, nonconvex optimization.

I. INTRODUCTION

Phase retrieval is an inverse problem that has many applications in engineering and applied physics [1, 2], including radar [3], X-ray crystallography [4], astronomical imaging [5] and speech processing [6], where the goal is to recover the signal from only the magnitude of linear measurements, such as the magnitude of its Fourier transform [7]. This paper focuses on cases where the measurements follow Poisson distributions.

In most previous works, the measurement vector $\mathbf{y} \in \mathbb{R}^M$ was assumed to have statistically independent ele-

ments following Gaussian distributions:

$$y_i \sim \mathcal{N}(|\mathbf{a}'_i \mathbf{x}|^2 + b_i, \sigma^2), \quad (1)$$

where $\mathbf{a}'_i \in \mathbb{C}^N$ denotes the i th row of the system matrix $\mathbf{A} \in \mathbb{C}^{M \times N}$, $\mathbf{x} \in \mathbb{F}^N$ denotes the true unknown signal, and b_i denotes a known mean background signal for the i th measurement, where $i = 1, \dots, M$. Here the field $\mathbb{F} = \mathbb{R}$ or $\mathbb{F} = \mathbb{C}$ depending on whether \mathbf{x} is known to be real or complex. For this Gaussian noise model, the ML estimate of \mathbf{x} corresponds to the following nonconvex optimization problem

$$\hat{\mathbf{x}} = \underset{\mathbf{x} \in \mathbb{F}^N}{\operatorname{argmin}} g(\mathbf{x}), \quad g(\mathbf{x}) \triangleq \sum_i \left| y_i - b_i - |\mathbf{a}'_i \mathbf{x}|^2 \right|^2. \quad (2)$$

To solve (2), numerous algorithms have been proposed, such as Wirtinger Flow [8], Gerchberg Saxton [9] and majorize-minimize (MM) methods [7].

However, in some low-photon count applications [10–16], a Poisson noise model is more appropriate:

$$y_i \sim \text{Poisson}(|\mathbf{a}'_i \mathbf{x}|^2 + b_i), \quad (3)$$

where here $b_i \geq 0$ denotes known mean background counts for the i th measurement, e.g., as arising from dark current [17]. The optimization problem for ML estimation under the Poisson model (3) is:

$$\hat{\mathbf{x}} = \underset{\mathbf{x} \in \mathbb{F}^N}{\operatorname{argmin}} f(\mathbf{x}), \quad f(\mathbf{x}) \triangleq \sum_i \psi(\mathbf{a}'_i \mathbf{x}; y_i, b_i),$$

$$\psi(v; y, b) \triangleq (|v|^2 + b) - y \log(|v|^2 + b). \quad (4)$$

One can verify that the function

$$h(r; y, b) \triangleq (r^2 + b) - y \log(r^2 + b), \quad r \in \mathbb{R}, \quad (5)$$

is nonconvex when $0 < b < y$. That property, combined with the modulus within the logarithm in (4), makes (4) a challenging optimization problem.

Similar problems for the case $b = 0$ have been considered previously [18–21], so this paper will mainly focus on the case when $b > 0$. Moreover, many optical sensors also have Gaussian readout noise [22, 23], so a more precise model would consider a sum of Gaussian and Poisson noise. However, the log likelihood for a Poisson plus Gaussian distribution is complicated, so a common approximation is to use a shifted Poisson

Zongyu Li and Jeffrey A. Fessler are with Department of Electrical Engineering and Computer Science, University of Michigan, Ann Arbor, MI 48109-2122 (e-mail: zonyul@umich.edu, fessler@umich.edu).

Kenneth Lange is with Departments of Computational Medicine, Human Genetics, and Statistics, University of California, Los Angeles, CA 90095 (e-mail: klange@ucla.edu).

Research supported in part by USPHS grants GM53275 and HG006139, and by NSF Grant IIS 1838179. Code for reproducing the results will be available on <https://github.com/ZongyuLi-umich> after the paper is accepted.

model [24] that also leads to the cost function in (4). An alternative to the shifted Poisson model could be to work with an unbiased inverse transformation of a generalized Anscombe transform approximation [25]. This paper will focus on algorithms for the pure Poisson noise model (3); algorithms for a Poisson plus Gaussian noise model can be an interesting direction for future work.

We treat $0 \log 0$ as being 0 in (4) because a Poisson random variable with zero mean can only take the value 0. In other words, if $|v| = b = 0$, then $\psi(v; y, b) = 0$. With this assumption, one can verify that ψ has a well-defined ascent direction (negative of descent direction [26]):

$$\dot{\psi}(v; y, b) = 2v \left(1 - \frac{y}{|v|^2 + b} \right), \quad v \in \mathbb{C}. \quad (6)$$

In most real-world applications, background counts are rarely to be zero (e.g., considering naturally occurring background radiation). When $b > 0$, one can derive the following upper bound for the magnitude of the second-order ascent direction of ψ :

$$\begin{aligned} \ddot{\psi}(v; y, b) &= \text{sign}(v) \left(2 + 2y \frac{|v|^2 - b}{(|v|^2 + b)^2} \right), \\ |\ddot{\psi}(v; y, b)| &\leq 2 + \frac{y}{4b}. \end{aligned} \quad (7)$$

This bounded curvature property enables us to construct a quadratic majorizer for (4) and derive an MM algorithm [27]. To handle the case when $b = 0$, we also investigated an alternating direction method of multipliers (ADMM) (Section III-C), adopted from [28].

The rest of this paper is organized as follows. Section II gives a brief overview of classical algorithms like WF and GS for phase retrieval. Section III introduces algorithms for Poisson phase retrieval, namely a modified Wirtinger flow method, a new MM approach, and a small variation of the ADMM algorithm of [28]. Section IV illustrates the implementation details of algorithms discussed in Section III. Section V provides numerical results using simulated data under different experimental settings.

Notation: Bold upper/lower case letters (e.g., \mathbf{A} , \mathbf{x} , \mathbf{y} , \mathbf{b}) denote matrices and column vectors, respectively. Italics (e.g., μ , y , b) denote scalars. y_i and b_i denote the i th element in vector \mathbf{y} and \mathbf{b} , respectively. \mathbb{R}^N and \mathbb{C}^N denote N -dimensional real/complex normed vector space, respectively. $(\cdot)^*$ denotes the complex conjugate and $(\cdot)'$ denotes Hermitian transpose. $\text{diag}\{\cdot\}$ is a diagonal matrix constructed from a column vector. Unless otherwise defined, a subscript denotes outer iterations and superscript denotes the inner iterations, respectively.

For example, \mathbf{x}_k^i denote the estimate of \mathbf{x} at the i th inner iteration of the k th outer iteration. For gradients associated with complex numbers/vectors, the notation $\dot{\psi}(\cdot)$ and $\nabla(\cdot)$, should be considered as an ascent direction, not as a derivative.

II. CLASSIC METHODS FOR GAUSSIAN MODEL

A. Wirtinger Flow

The classic Wirtinger flow algorithm for gradient descent of the Gaussian cost function (2) uses the gradient¹ [8]:

$$\nabla g(\mathbf{x}) = 4\mathbf{A}' \text{diag}\{|\mathbf{Ax}|^2 - \mathbf{y} + \mathbf{b}\} \mathbf{Ax}. \quad (8)$$

To descend the cost function, [8] used a heuristic where μ is rather small at the first few iterations and gradually becomes larger as the iterations count increases. The intuition is that the noise is large at the early iterations and it decreases as the iteration counts increase. A drawback of that approach is that one needs to select hyper-parameters that control the growing speed of μ . An alternative approach is to perform backtracking for μ in each iteration [7], by reducing μ until the cost function decreases sufficiently. However, this approach can increase the compute time of the algorithm due to the variable number of inner iterations.

B. Gerchberg Saxton

An alternative to the intensity model (2) is the magnitude model that assumes the recorded values are the square root of \mathbf{y} . To optimize the cost function based on the magnitude model, one can introduce a new variable $\boldsymbol{\theta}$ to represent the phase, leading to the following optimization problem:

$$\begin{aligned} \hat{\mathbf{x}}, \hat{\boldsymbol{\theta}} &= \underset{\mathbf{x} \in \mathbb{R}^N, \boldsymbol{\theta} \in \mathbb{C}^N}{\text{argmin}} \|\mathbf{Ax} - \text{diag}\{\sqrt{\max(\mathbf{y} - \mathbf{b}, \mathbf{0})}\} \boldsymbol{\theta}\|_2^2, \\ \text{subject to } |\theta_i| &= 1, \quad i = 1, \dots, N. \end{aligned} \quad (9)$$

To solve (9), one classic approach is the Gerchberg Saxton (GS) algorithm [9] that alternatively updates \mathbf{x} and $\boldsymbol{\theta}$ in each iteration. WF and GS are two classic methods for phase retrieval under the Gaussian noise model.

A potential drawback of these classic methods is that they are inapplicable [29] to accommodate non-smooth regularizers, e.g., $\|\mathbf{T}\mathbf{x}\|_1$, where \mathbf{T} is a transform matrix. In such cases, we have to seek for other algorithms, i.e., MM and ADMM.

¹Please note that if $\mathbf{x} \in \mathbb{R}^N$, then all gradients w.r.t. \mathbf{x} in this paper should be real and hence should only keep the real part.

III. METHODS FOR POISSON MODEL

A. Wirtinger Flow for Poisson Model

To generalize the Wirtinger flow algorithm to the Poisson cost function (4), the most direct approach simply replaces the gradient (8) by (6) in the WF framework [30] and performs backtracking to find the step-size μ , as in [7]. We propose a faster alternative next.

1) *Observed Fisher Information for Step Size:* We propose to make a quadratic approximation along the gradient direction of the cost function at each iteration, and then apply one step of Newton's method to minimize that 1D quadratic. Because computing the Hessian can be computationally expensive in large-scale problems, we replace the Hessian by the observed Fisher information when applying Newton's method [31].

Specifically, we first approximate the 1D line search problem associated with (4) by the following Taylor series

$$\begin{aligned} \mu_k &= \underset{\mu \in \mathbb{R}}{\operatorname{argmin}} f_k(\mu), \\ f_k(\mu) &\triangleq f(\mathbf{x}_k + \mu \nabla f(\mathbf{x}_k)) \approx f(\mathbf{x}_k) + \|\nabla f(\mathbf{x}_k)\|_2^2 \mu \\ &\quad + \frac{1}{2} \nabla f(\mathbf{x}_k)' \nabla^2 f(\mathbf{x}_k) \nabla f(\mathbf{x}_k) \mu^2, \end{aligned} \quad (10)$$

where one can verify that the minimizer is

$$\mu_k = -\frac{\|\nabla f(\mathbf{x}_k)\|_2^2}{\operatorname{real}\{\nabla f(\mathbf{x}_k)' \nabla^2 f(\mathbf{x}_k) \nabla f(\mathbf{x}_k)\}}. \quad (11)$$

We next approximate the Hessian matrix $\nabla^2 f(\mathbf{x})$ using the observed Fisher information matrix associated with ML estimation:

$$\begin{aligned} \nabla^2 f(\mathbf{x}) &\approx \mathbf{I}(\mathbf{x}, \mathbf{b}) \\ &\triangleq \mathbb{E}_{\mathbf{y}} \left[(\nabla f(\mathbf{x}; \mathbf{y}, \mathbf{b})) (\nabla f(\mathbf{x}; \mathbf{y}, \mathbf{b}))' \middle| \mathbf{x}, \mathbf{b} \right] \\ &= \mathbf{A}' \mathbb{E}_{\mathbf{y}} \left[(\psi(\mathbf{v}; \mathbf{y}, \mathbf{b})) (\psi(\mathbf{v}; \mathbf{y}, \mathbf{b}))' \middle| \mathbf{v}, \mathbf{b} \right] \mathbf{A}, \end{aligned} \quad (12)$$

where $\psi(\cdot)$ denotes element-wise application of the function ψ to its first argument (as in the Julia language). One can verify that the marginal Fisher information for a single term $\psi(\mathbf{v}; \mathbf{y}, \mathbf{b})$ is

$$\begin{aligned} \bar{I}(v, b) &= \mathbb{E}_{\mathbf{y}} \left[|\psi(\mathbf{v}; \mathbf{y}, \mathbf{b})|^2 \middle| v, b \right] \\ &= \frac{4|v|^2}{|v|^2 + b}, \quad v \in \mathbb{C}, \quad b > 0. \end{aligned} \quad (13)$$

Substituting (13) into (12) and then substituting (12) into (11) yields the simplified step-size expression

$$\mu_k \triangleq -\frac{\|\nabla f(\mathbf{x}_k)\|_2^2}{\mathbf{d}_k' \operatorname{diag}\{\bar{I}(\mathbf{d}_k, \mathbf{b})\} \mathbf{d}_k} \in \mathbb{R}, \quad (14)$$

where $\mathbf{d}_k \triangleq \mathbf{A} \nabla f(\mathbf{x}_k)$. (Careful implementation avoids redundant matrix-vector products.)

Similarly, the marginal Fisher information for the scalar case of the Gaussian cost function (2) is

$$I(v, b) = 16|v|^2(|v|^2 + b), \quad v \in \mathbb{C}, \quad b \geq 0. \quad (15)$$

Substituting (15) into (14), one can also derive a convenient step size μ_k for the WF algorithm for the Gaussian model (2) using its observed Fisher information to approximate the exact Hessian. This approach removes all tuning parameters other than number of iterations. In addition, using the observed Fisher information leads to a larger step size than using the best Lipschitz constant, i.e., $\max\{2 + \mathbf{y}/(4\mathbf{b})\}$ when $\mathbf{b} > 0$, accelerating convergence.

2) *Truncated Wirtinger Flow:* To potentially reduce the computational error in optimization due to measurement noise, reference [20] proposed a truncated Wirtinger flow (TWF) approach that uses only those measurements satisfying a threshold criterion to calculate the Wirtinger flow gradient. In particular, the threshold criterion [11] is defined as

$$|y_i - |\mathbf{a}_i' \mathbf{x}|^2| \leq a^h \frac{\|\mathbf{y} - |\mathbf{A}\mathbf{x}|^2\|_1}{M} \cdot \frac{|\mathbf{a}_i' \mathbf{x}|^2}{\|\mathbf{x}\|_2^2}, \quad (16)$$

where a^h is a user-defined parameter that controls the threshold value. When a^h is chosen appropriately, y_i values that do not satisfy (16) will be truncated when calculating the gradient, to try to reduce noise.

Algorithm 1 summarizes the (truncated) Wirtinger flow algorithm for the Poisson model that uses Fisher information for step size and optional gradient truncation for noise reduction. The results in Section V used the observed Fisher information for step size to accelerate both the Gaussian and Poisson WF methods, but did not use truncation, as explained in Section IV.

B. An MM Approach with a Quadratic Majorizer

A majorize-minimize (MM) algorithm [32] is a generalization of the expectation-maximization (EM) algorithm that solves an optimization problem by iteratively constructing and solving simpler surrogate optimization problems. Quadratic majorizers are very common in MM algorithms because they have closed-form solutions and are well-suited to conjugate gradient methods.

When $b = 0$, one can verify $\bar{\psi}$ has a singularity at $v = 0$, which means ψ is not Lipschitz differentiable, so we need to pursue other algorithms for this case, as

Algorithm 1: Wirtinger flow for the Poisson model

Input: $\mathbf{A}, \mathbf{y}, \mathbf{b}$ and n (number of iterations)

 Initialize: $\mathbf{x}_0 \leftarrow$ random Gaussian vector

for $k = 0, \dots, n - 1$ **do**

 if *gradient is truncated* **then**

 $\mathcal{T} \leftarrow$ indices satisfying (16)

 $\nabla f(\mathbf{x}_k) = \mathbf{A}'_{\mathcal{T}} \dot{\psi}([\mathbf{A}\mathbf{x}_k]_{\mathcal{T}}; \mathbf{y}_{\mathcal{T}}, \mathbf{b}_{\mathcal{T}})$

 else

 $\nabla f(\mathbf{x}_k) = \mathbf{A}' \dot{\psi}(\mathbf{A}\mathbf{x}_k; \mathbf{y}, \mathbf{b})$

 end

 $I(v, b) = 4|v|^2 / (|v|^2 + b)$

 $\mathbf{d}_k = \mathbf{A} \nabla f(\mathbf{x}_k)$

 $\mu_k = -\|\nabla f(\mathbf{x}_k)\|_2^2 / (\mathbf{d}_k' \text{diag}\{\bar{I}(\mathbf{d}_k, \mathbf{b})\} \mathbf{d}_k)$

 $\mathbf{x}_{k+1} = \mathbf{x}_k + \mu_k \nabla f(\mathbf{x}_k)$

 $(\mathbf{A}\mathbf{x}_{k+1}) = (\mathbf{A}\mathbf{x}_k) + \mu_k \mathbf{d}_k$
end
Output: \mathbf{x}_n

discussed in a subsequent section. In contrast, if $b > 0$, one can construct a quadratic majorizer for the Poisson ML cost function (4) of the form

$$q(\mathbf{x}; \mathbf{x}_k) \triangleq f(\mathbf{x}_k) + \text{real}\left\{(\mathbf{x} - \mathbf{x}_k)' \mathbf{A}' \dot{\psi}(\mathbf{A}\mathbf{x}_k; \mathbf{y}, \mathbf{b})\right\} + \frac{1}{2}(\mathbf{x} - \mathbf{x}_k)' \mathbf{A}' \mathbf{W} \mathbf{A}(\mathbf{x} - \mathbf{x}_k), \quad (17)$$

where \mathbf{W} denotes a diagonal curvature matrix. From (7), one choice of \mathbf{W} uses the maximum of $\ddot{\psi}$:

$$\mathbf{W}_{\max} \triangleq \text{diag}\{2 + \mathbf{y}/(4\mathbf{b})\} \in \mathbb{R}^{M \times M}. \quad (18)$$

However, this curvature matrix is suboptimal because the curvature of quadratic majorizers of $\psi(v; \cdot)$ varies with $v = [\mathbf{A}\mathbf{x}_k]_i$. For example, when $|v| \rightarrow \infty$, then (4) is dominated by the quadratic term having curvature 2 so that if y is large and b is small, then the majorizing curvature can be much greater than the optimal curvature 2. Thus, instead of using \mathbf{W}_{\max} , we propose to use the following improved curvature:

$$\mathbf{W}_{\text{imp}} \triangleq \text{diag}\{c(\mathbf{A}\mathbf{x}_k; \mathbf{y}, \mathbf{b})\} \in \mathbb{R}^{M \times M},$$

$$c(s; y, b) \triangleq \begin{cases} \ddot{\psi}\left(\frac{b + \sqrt{b^2 + b|s|^2}}{|s|}; y, b\right), & s \neq 0, \\ 2, & s = 0. \end{cases} \quad (19)$$

One can verify $\lim_{s \rightarrow 0} c(s; y, b) = 2$ so (19) is continuous over $s \in \mathbb{C}$. Appendix A proves that (19) provides a majorizer in (17) and is an improved curvature, though it is not necessarily the sharpest possible [33].

For the ML case where constraints or regularizers are absent, the quadratic majorizer (17) associated with (18) or (19) leads to the following MM update:

$$\begin{aligned} \mathbf{x}_{k+1} &= \underset{\mathbf{x} \in \mathbb{R}^N}{\text{argmin}} q(\mathbf{x}; \mathbf{x}_k) \\ &= \mathbf{x}_k - (\mathbf{A}' \mathbf{W} \mathbf{A})^{-1} \mathbf{A}' \dot{\psi}(\mathbf{A}\mathbf{x}_k; \mathbf{y}, \mathbf{b}). \end{aligned} \quad (20)$$

If $\mathbf{x} \in \mathbb{R}^N$, then $\mathbf{A}' \mathbf{W} \mathbf{A}$ and $\mathbf{A}' \dot{\psi}(\mathbf{A}\mathbf{x}_k; \mathbf{y}, \mathbf{b})$ in (20) should be $\text{real}\{\mathbf{A}' \mathbf{W} \mathbf{A}\}$ and $\text{real}\{\mathbf{A}' \dot{\psi}(\mathbf{A}\mathbf{x}_k; \mathbf{y}, \mathbf{b})\}$, instead.

When N is large the matrix inverse operation in (20) is impractical, so one alternative way is to run a few inner iterations of conjugate gradient (CG) to descend the quadratic majorizer and hence descend the original cost function. When regularizers are included in the cost function (4), one can use the quadratic majorizer as the foundation for a proximal method if the regularizer is prox-friendly. Here we choose the regularizer as $\beta \|\mathbf{T}\mathbf{x}\|_1$, where $\mathbf{T} \in \mathbb{C}^{K \times N}$ is a transform matrix. Based on (17), the minimization step of a MM algorithm for the regularized optimization problem is

$$\mathbf{x}_{k+1} = \underset{\mathbf{x} \in \mathbb{R}^N}{\text{argmin}} q(\mathbf{x}; \mathbf{x}_k) + \beta \|\mathbf{T}\mathbf{x}\|_1. \quad (21)$$

If \mathbf{T} is prox-friendly, e.g., an orthogonal discrete wavelet transform (ODWT) matrix, then one can apply proximal gradient methods [34–36] to solve (21).

If \mathbf{T} is not prox-friendly, e.g., the finite difference matrix used in total variation (TV) regularization, then we can replace (21) by a two-block cost function:

$$\begin{aligned} \mathbf{x}_{k+1}, \mathbf{z}_{k+1} &= \underset{\mathbf{x} \in \mathbb{R}^N, \mathbf{z} \in \mathbb{C}^K}{\text{argmin}} Q_k(\mathbf{x}, \mathbf{z}), \\ Q_k(\mathbf{x}, \mathbf{z}) &\triangleq q(\mathbf{x}; \mathbf{x}_k) + \beta \left(\frac{1}{2} \|\mathbf{T}\mathbf{x} - \mathbf{z}\|_2^2 + \alpha \|\mathbf{z}\|_1 \right), \end{aligned} \quad (22)$$

where one can alternatively update \mathbf{x} and \mathbf{z} . The \mathbf{x} update uses the closed-form solution that involves matrix inverse or conjugate gradient. The \mathbf{z} update is simply a soft-thresholding operation.

Algorithm 2 summarizes our MM algorithm with quadratic majorizer using the improved curvature (19).

C. ADMM

To handle the case when $b = 0$, we investigated an ADMM algorithm with variable splitting $v_i = \mathbf{a}'_i \mathbf{x}$. This ADMM algorithm generalizes to $b_i > 0$ by a simple modification of the v_i update. Previous work [28] also applied ADMM to a Poisson ML cost function (for $b_i = 0$) for a total-variation (TV) regularizer, with separate variable splitting for both the log-likelihood and for the gradient operator. Compared to the ADMM in [28], our ADMM variant also considered $b_i > 0$ case and is slightly simpler to implement, but is otherwise somewhat similar to [28]. The ADMM is included here primarily for completeness i.e., as an alternative for MM in the $b_i = 0$ case.

Algorithm 2: MM algorithm for the Poisson model**Input:** \mathbf{A} , \mathbf{y} , \mathbf{b} and n (number of iterations)Initialize: $\mathbf{x}_0 \leftarrow$ random Gaussian vector**for** $k = 0, \dots, n - 1$ **do** Build $q(\mathbf{x}; \mathbf{x}_k)$ (17) using \mathbf{W}_{imp} (19) **if** *cost function is regularized* **then** **if** T is prox-friendly **then** Update \mathbf{x}_k by (21) using POGM **else** Update \mathbf{x}_k by (22) using CG and soft-thresholding **end** **else** Update \mathbf{x}_k using CG **end****end****Output:** \mathbf{x}_n

With variable splitting $v_i = \mathbf{a}'_i \mathbf{x}$, an augmented linearized Lagrangian of (4) when $b_i = 0$ is given by

$$L_\rho(\mathbf{v}, \mathbf{x}; \boldsymbol{\eta}, \rho) = \sum_i \left[(|v_i|^2) - y_i \log(|v_i|^2) \right] + \frac{\rho}{2} \sum_i \left[|v_i - \mathbf{a}'_i \mathbf{x} + \eta_i|^2 - |\eta_i|^2 \right], \quad (23)$$

where $\boldsymbol{\eta}$ is the dual variable and $\rho > 0$ denotes the AL penalty parameter.

We followed the order of first updating \mathbf{v} , then \mathbf{x} and finally $\boldsymbol{\eta}$. The updates for the phase and magnitude of \mathbf{v} are separable. In particular, the update for the phase of \mathbf{v} is

$$\text{sign}(\mathbf{v}_{k+1}) = \text{sign}(\mathbf{A}\mathbf{x}_k - \boldsymbol{\eta}_k). \quad (24)$$

To update the magnitude of \mathbf{v} , similar to [28], set $t_i = |\mathbf{a}'_i \mathbf{x}_k - \eta_i|$; then the update of component $|v_i|$ is given by the following nonnegative solution of a quadratic polynomial:

$$|v_i| = \frac{\rho t_i + \sqrt{\rho^2 t_i^2 + 8y_i(2 + \rho)}}{2(2 + \rho)}. \quad (25)$$

Again, in the unregularized case, the \mathbf{x} update is a simple least square (LS) problem that can be optimized by CG or the following operation (26) involving matrix inverse.

$$\mathbf{x}_{k+1} = (\mathbf{A}'\mathbf{A})^{-1} \mathbf{A}'(\mathbf{v}_{k+1} + \boldsymbol{\eta}_k), \quad (26)$$

Again, if $\mathbf{x} \in \mathbb{R}^N$, then $\mathbf{A}'\mathbf{A}$ and $\mathbf{A}'(\mathbf{v}_{k+1} + \boldsymbol{\eta}_k)$ in (26) should be $\text{real}\{\mathbf{A}'\mathbf{A}\}$ and $\text{real}\{\mathbf{A}'(\mathbf{v}_{k+1} + \boldsymbol{\eta}_k)\}$, instead. When we consider a non-smooth regularizer $\|\mathbf{T}\mathbf{x}\|_1$, the \mathbf{x} update becomes either

$$\mathbf{x}_{k+1} = \underset{\mathbf{x} \in \mathbb{R}^N}{\text{argmin}} \frac{\rho}{2} \|\mathbf{A}\mathbf{x} - \mathbf{v}_{k+1} - \boldsymbol{\eta}_k\|_2^2 + \beta \|\mathbf{T}\mathbf{x}\|_1. \quad (27)$$

or

$$\mathbf{x}_{k+1}, \mathbf{z}_{k+1} = \underset{\mathbf{x} \in \mathbb{F}^N, \mathbf{z} \in \mathbb{C}^K}{\text{argmin}} \frac{\rho}{2} \|\mathbf{A}\mathbf{x} - \mathbf{v}_{k+1} - \boldsymbol{\eta}_k\|_2^2 + \beta \left(\frac{1}{2} \|\mathbf{T}\mathbf{x} - \mathbf{z}\|_2^2 + \alpha \|\mathbf{z}\|_1 \right), \quad (28)$$

depending on if T is prox-friendly.

The dual variable $\boldsymbol{\eta}$ ascent update is simply [37]:

$$\boldsymbol{\eta}_{k+1} = \boldsymbol{\eta}_k + (\mathbf{v}_{k+1} - \mathbf{A}\mathbf{x}_{k+1}). \quad (29)$$

For the case $b_i > 0$, everything is the same as the case $b_i = 0$ except the update for $|v_i|$, for which one can verify the $|v_i|$ is a positive root of the following cubic polynomial

$$0 = (2 + \rho)|v_i|^3 - \rho t_i |v_i|^2 + (2b_i - 2y_i + \rho b_i)|v_i| - \rho b_i t_i. \quad (30)$$

Owing to the intermediate value theorem and the non-negativity of ρ , b_i , t_i , this cubic (30) can only possess one or three positive real roots. If the cubic has one positive root, then the update of $|v_i|$ is simply to assign the single positive root. If the cubic has three positive roots, we choose the root that minimizes the following Lagrangian term based on (31):

$$(|v_i|^2 + b_i) - y_i \log(|v_i|^2 + b_i) + \frac{\rho}{2} (|v_i| - t_i)^2. \quad (31)$$

A natural extension is to vary AL penalty parameter along with the variable update every few iterations. Reference [37] considered the magnitude of primal residual $\mathbf{r}_{k+1} = \mathbf{A}\mathbf{x}_{k+1} - \mathbf{v}_{k+1}$ and dual residual $\mathbf{s}_{k+1} = \rho \mathbf{A}'(\mathbf{v}_{k+1} - \mathbf{v}_k)$, as a principle to select penalty parameter to potentially improve convergence for convex optimization problems. However, for non-convex problems, the penalty parameter ρ is preferred to be sufficiently large to enable the convergence of ADMM algorithm [38]. Thus, we used the following heuristic to update ρ every 10 iterations:

$$\rho_{k+1} = \begin{cases} 2\rho_k, & \|r_k\| > 10\|s_k\| \\ \rho_k/2, & \|s_k\| > 100\rho_k\|r_k\| \\ \rho_k, & \text{otherwise.} \end{cases} \quad (32)$$

Algorithm 3 summarizes the ADMM algorithm described above.

IV. IMPLEMENTATION DETAILS

This section introduces the implementation details of algorithms discussed in the previous section and our experimental setup for the numerical simulation (Section V). Due to the page limit, Sections IV-A, IV-B and IV-C directly state conclusions without supporting figures. See the supplemental materials for these figures.

Algorithm 3: ADMM algorithm for the Poisson model

Input: \mathbf{A} , \mathbf{y} , \mathbf{b} and n (number of iterations)

Initialize:

 $\mathbf{x}_0 \leftarrow$ random Gaussian vector

 $\mathbf{v}_0 \leftarrow \mathbf{A}\mathbf{x}_0$
 $\boldsymbol{\eta}_0 \leftarrow \mathbf{v}_0 - \mathbf{A}\mathbf{x}_0$
for $k = 0, \dots, n - 1$ **do**

 Update $\text{sign}(\mathbf{v}_k)$ by (24)

if $b_i = 0$ **then**

 | Update $|\mathbf{v}_k|$ by (25)

else

 | Update $|\mathbf{v}_k|$ by selecting root based on (31)

end
if cost function is regularized **then**
if T is prox-friendly **then**

 | Update \mathbf{x}_k by (27) using POGM

else

 | Update \mathbf{x}_k by (28) using CG and soft-thresholding

end
else

 | Update \mathbf{x}_k using CG

end

 Update $\boldsymbol{\eta}_k$ by (29)

end
Output: \mathbf{x}_n

A. Solve Quadratic Problems

As discussed in the previous section, performing matrix inverse is impractical in large scale problems. Moreover, interestingly, even in small/medium scale problems, we found that running few iterations of CG was somewhat (or much) faster than performing matrix inverse (back slash in Julia) yet could give almost the same reconstructed quality. Thus, we used the CG algorithm instead of performing matrix inverse whenever solving a least squares problem, i.e., in equation (20), (22), (26), (28) shown in Section III. In particular, we ran 3 iterations of CG in the first 10 outer iterations (out of 200 iterations) and only 1 CG update (equivalent to steepest gradient descent) after that.

B. Observed Fisher Information vs. Line Search

We compared the convergence speed, i.e., how fast an algorithm can decrease the NRMSE, between WF using the observed Fisher information and using line search for step size. Using the observed Fisher information for step size is faster in time than using a line search (see supplemental materials) whereas the latter can decrease NRMSE more within each (slower) iteration. Therefore,

the experiments in Section V used the observed Fisher information for step size in WF algorithm.

C. Truncated Wirtinger Flow?

TWF was commonly used in phase retrieval applications where the measurements follow independent Gaussian distribution. In our experiments, however, we did not apply truncation for the following reasons.

- 1) We did not observe any improved reconstruction quality for various setting of a^h compared to WF. We found that the reconstructed error (NRMSE) of TWF decreases almost monotonically as the truncation threshold parameter a^h in (16) becomes larger, which is consistent with results in [11]. Furthermore, to achieve a comparable reconstruction quality with the non-truncated WF, one needs to keep about 95% of indices, indicating that almost all the measurements contribute to the recovery, and therefore should not be truncated, under the Poisson noise model.
- 2) TWF can be computationally inefficient because it requires computing the truncated indices in each iteration, especially when both the iteration number and M are large.

D. MM for DFT Matrix Setting

When \mathbf{A} is a DFT matrix, we conjectured that the dynamic range of the y_i values can be very wide, leading to an ill-conditioned curvature matrix \mathbf{W} . In particular, the curvature changes dramatically across different coordinates, and the MM algorithm based on a quadratic majorizer using the maximum or improved curvature can converge very slowly. Thus, for the DFT case we imposed a threshold on the elements of the curvature matrix \mathbf{W} as follows: $\tilde{\mathbf{W}} = \min(\mathbf{W}, \mathbf{W}_\mu + 3\mathbf{W}_\sigma)$, where \mathbf{W}_μ and \mathbf{W}_σ denote the mean and the standard deviation of the diagonal elements of the original \mathbf{W} , respectively. We used $\tilde{\mathbf{W}}$ to construct quadratic “majorizers” for the DFT case. It would be computationally expensive to directly compute the best Lipschitz constant ($\mathcal{L} = \|\mathbf{A}'\tilde{\mathbf{W}}\mathbf{A}\|_2$) every time \mathbf{W} changes, so we used $\mathcal{L} = c_{\text{dft}}^2 \tilde{N}^2 L \|\mathbf{W}\|_2$ in MM algorithms, where one can verify $\|\mathbf{A}'\mathbf{A}\|_2 \leq c_{\text{dft}}^2 \tilde{N}^2 L$, where c_{dft} is the scaling factor applied to \mathbf{A} .

E. Ambiguities

To handle the phase ambiguity (all the algorithms can recover the signal only to within a constant phase shift

due to the loss of global phase information), we used the following normalized root mean square error (NRMSE) metric [7] to evaluate all the algorithms:

$$\text{NRMSE} = \frac{\|\hat{\mathbf{x}} - \mathbf{x}_{\text{true}} e^{i\phi}\|_2}{\|\mathbf{x}_{\text{true}}\|_2}, \quad e^{i\phi} = \text{sign}(\mathbf{x}'_{\text{true}} \hat{\mathbf{x}}), \quad (33)$$

where $\hat{\mathbf{x}}$ and \mathbf{x}_{true} denote the reconstructed signal/image and the true signal/image, respectively.

In the DFT matrix setting, there are more ambiguities, such as circular shift and conjugate inversion [39]. To circumvent these ambiguities, one method is to use several different masks that introduce redundancy in the measurement vector \mathbf{y} . In particular, when \mathbf{A} is DFT matrix, in the classical Fourier phase retrieval problem setting [40], \mathbf{y} has elements given for $\tilde{n} = 0, \dots, \tilde{N} - 1$ by

$$y[\tilde{n}] = \left| \sum_{n=0}^{N-1} x[n] e^{-i2\pi n \tilde{n} / \tilde{N}} \right|^2 + b[\tilde{n}], \quad (34)$$

where $\tilde{N} = 2N - 1$ (here we consider the over-sampled case). After introducing redundant masks, the measurement model becomes

$$y_l[\tilde{n}] = \left| \sum_{n=0}^{N-1} x[n] D_l[n] e^{-i2\pi n \tilde{n} / \tilde{N}} \right|^2 + b_l[\tilde{n}], \quad (35)$$

where $y_l \in \mathbb{R}^{\tilde{N}}$ for $i = 1, \dots, L$ and D_l denotes the l th of L masks. Here $M = L\tilde{N}$. Our experiment used $L = 21$ masks to define the overall system matrix \mathbf{A} , where the first mask has full sampling and the remaining 20 have sampling rate 0.5 with random sampling patterns.

F. Summary

Considering all the factors discussed above, the algorithms compared in our experiments are introduced and abbreviated as follows.

- WF-Gaussian and WF-Poisson: non-truncated Wirtinger Flow algorithms based on the Gaussian/Poisson model, using the observed Fisher information to select the step size.
- GS: the Gerchberg Saxton algorithm based on the Gaussian model (9).
- LSMM: Unregularized MM algorithm with quadratic majorizer using the improved curvature.
- ADMM: Unregularized ADMM algorithm with adaptive AL penalty parameter (ρ) that is initialized as 16.
- Regularized MM and ADMM: These algorithms use the regularizer $\beta\|\mathbf{T}\mathbf{x}\|_1$, where \mathbf{T} denotes the finite difference matrix or ODWT matrix. The regu-

larized ADMM uses the same AL penalty parameter strategy as the unregularized ADMM.

We ran all algorithms for 200 iterations on a server with Ubuntu 16.04 LTS operating system having Intel(R) Xeon(R) CPU E5-2698 v4 @ 2.20GHz and 251 GB memory. We investigated 2 different system matrix \mathbf{A} : complex random Gaussian matrix and discrete Fourier transform (DFT) matrix. All elements in the measurement vector \mathbf{y} were simulated to follow independent Poisson distributions per (3).

V. NUMERICAL SIMULATIONS RESULTS

This section reports numerical simulations that demonstrate that using the Poisson log likelihood improves the quality of the estimates under various experimental settings and compare the convergence rates of the various algorithms.

A. Random Gaussian Sensing Matrix

First we consider the case when all the elements in the system matrix \mathbf{A} are independent random variables following a complex Gaussian distribution. We scaled \mathbf{A} by a constant such that the average of $|\mathbf{a}'_i \mathbf{x}_{\text{true}}|^2$ is 2. The mean background counts \mathbf{b} were set to 0.1 (a constant vector). Here we exploit the piece-wise uniformity of the true signal, for which a natural choice for \mathbf{T} is finite differences, i.e., a discrete TV regularizer [28]. We denote the LSMM and ADMM algorithms using the TV regularizer as LSMM-TV and ADMM-TV, respectively. We chose the number of measurements M to range from 2500 to 10000. We repeated each experiment 50 times and averaged the results to reduce the effects of statistical randomness. We empirically chose the regularizer parameters $\beta = 32$ and $\alpha = 0.5$ in (22) and (28). We ran 3 iterations of CG to update \mathbf{x} in (22) and (28).

1) *True Signals*: We used a finite length ($N = 100$) signal as the true signal. It is a piece-wise constant complex signal whose real part and imaginary part are shown in Fig. 1.

2) *Accuracy Comparison*: Fig. 2 compares the NRMSE of all algorithms for $b_i > 0$ and $b_i = 0$, respectively. As expected, algorithms based on the Poisson model produce consistently better quality results (lower NRMSE) than algorithms based on the Gaussian model. In particular, LSMM, ADMM and WF Poisson overlapped together, perhaps they all converged to a global minimizer. In addition, improvements are more notable

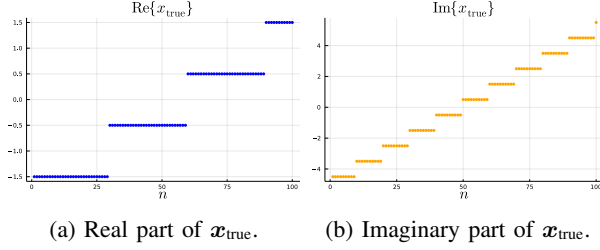


Fig. 1: The true signal used in simulations when \mathbf{A} is random Gaussian matrix.

for $b_i = 0$ than $b_i > 0$, possibly because $\mathbb{E}[\mathbf{y}]$ is even lower when $b_i = 0$ than $b_i > 0$, so the Gaussian model may perform even worse in that case. Furthermore, regularized algorithms (LSMM-TV and ADMM-TV) led to the lowest NRMSE and were less sensitive to the change of M than the unregularized algorithms, and improved NRMSE the most when $M = 2500$. This illustrates that the regularizers exploiting the assumed properties of the true signal can help the algorithms recover \mathbf{x} , i.e., perhaps by denoising through regularization, when the measurements are noisy or corrupted, and especially when the number of measurements is low.

3) *Speed Comparison:* Fig. 3 compares how quickly different algorithms decrease the NRMSE when the number of measurements is $M = 5000$. The regularized algorithms are slower because they involve inner-iterations. As expected, WF Poisson decreases NRMSE faster than WF Gaussian. Our reasons are as follows. Firstly, the Poisson model is more accurate than the Gaussian model and so as to its gradient. Secondly, the quadratic approximation fits better to (4) than (2) because (4) is more similar to a quadratic function, i.e., has bounded curvature when $b_i > 0$, whereas (2) is a quartic with unbounded curvature. For unregularized algorithms, the WF Poisson and GS decreased the NRMSE fastest while WF Poisson demonstrated higher reconstruction quality. For regularized algorithms the regularized LSMM much faster than regularized ADMM and even has comparable speed performance as the unregularized algorithms, but with notably improved reconstruction accuracy (lower NRMSE).

B. Discrete Fourier Transform Matrix

In many optical imaging applications, system matrix \mathbf{A} is often modeled with a DFT matrix. Here we scaled the DFT matrix \mathbf{A} by a constant c_{dft} so that the average of $|\mathbf{a}'_i \mathbf{x}_{\text{true}}|^2$ is 1 and the background counts vector \mathbf{b} was set to 0.1. Different from the previous section, here we exploited the fact that the detail coefficients of the discrete wavelet transform of the true image are sparse,

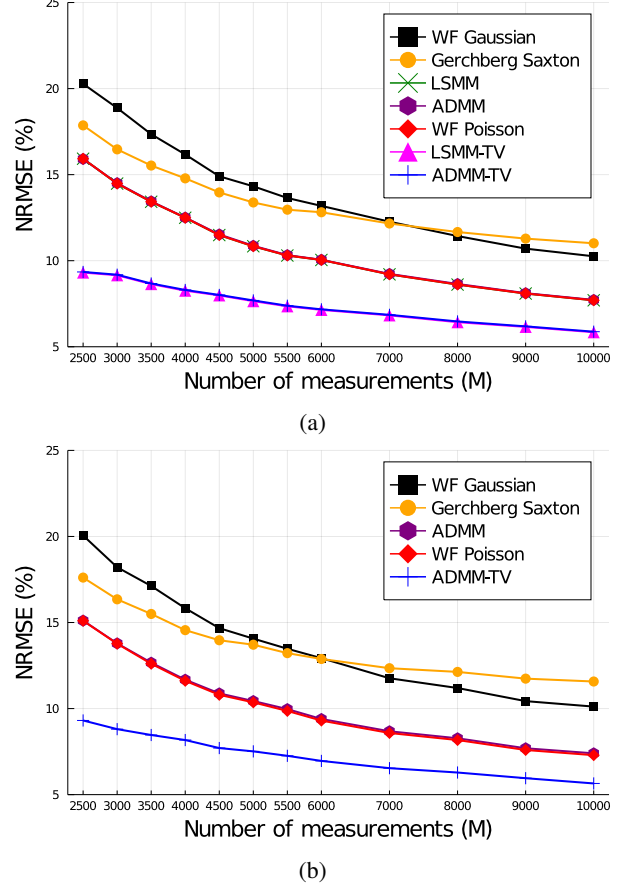


Fig. 2: NRMSE vs. number of measurements (M) when \mathbf{A} is random Gaussian, where (a) and (b) correspond to $b_i = 0.1$ and $b_i = 0$, respectively.

so we chose the matrix \mathbf{T} in the regularizer to be an ODWT matrix. Because the pixel values in an image cannot be negative, we initialize \mathbf{x} as a random vector following a uniform distribution on $[0, 1]$. We empirically chose the regularization parameter $\beta = 32$ in (21) and (27). We ran 10 inner iterations of POGM with adaptive restart [36] for each outer iteration.

1) *True Signals:* Our true images are an elegant “UM1817” image of size 64×64 and a Shepp-Logan phantom of size 256×256 . Pixel values for both two images range from 0 to 1.

2) *Accuracy Comparison:* Fig. 5 and Fig. 6 compare the images reconstructed by the WF, GS, MM and ADMM algorithms. Again, as expected, algorithms based on the Poisson model had better reconstruction quality than algorithms derived from Gaussian model. The regularized algorithms that exploit the assumed properties of the true image can further improve the reconstruction quality. Interestingly, our results showed that WF Gaussian algorithm failed to reconstruct the image. Firstly we thought

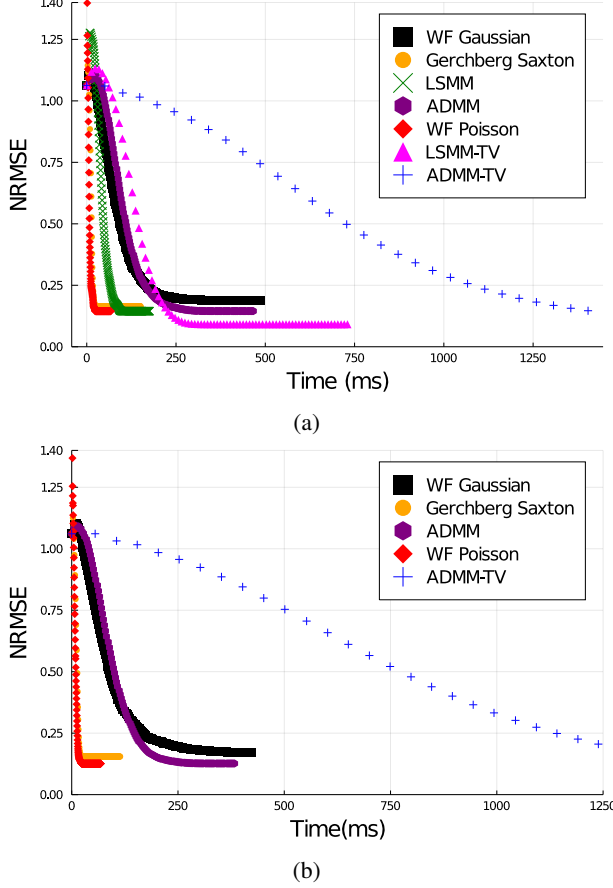


Fig. 3: NRMSE vs. time (ms) when \mathbf{A} is random Gaussian, $M = 5000$. Subfigure (a) and (b) correspond to $b_i = 0.1$ and $b_i = 0$, respectively.

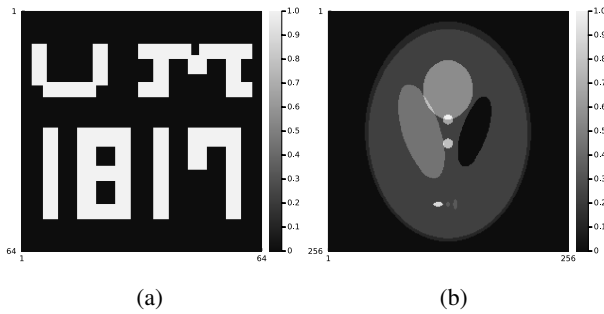


Fig. 4: Test true images for DFT matrix setting (Section V-B).

that there were bugs in our code for WF Gaussian algorithm, but then we checked the literature and found that in Qiu's paper [7], the WF-Gaussian algorithm was also shown to have very low recovery probability when \mathbf{A} is a DFT matrix, which was consistent with our finding. However, figuring out why WF Gaussian fails to reconstruct can be an interesting future work.

VI. CONCLUSION

This paper compares several algorithms including Wirtinger flow (WF), Gerchberg Saxton (GS), majorize-minimize (MM) and alternating direction method of multipliers (ADMM), for ML estimation and regularized ML estimation for phase retrieval from Poisson measurements. For the WF algorithm, instead of performing backtracking or using a heuristic step size, we proposed to use a quadratic approximation along the gradient direction and replace the Hessian by the observed Fisher information so that the step size can be computed efficiently without any tuning parameter. For the MM algorithm with quadratic majorizers, we proposed a curvature formula and proved that it is superior to the curvature built on the upper bound of the second derivative of the Poisson ML cost function, i.e., the Lipschitz constant of its derivative.

Simulation results showed that the ML estimates based on the Poisson model (WF Poisson, MM, ADMM) yielded consistently lower NRMSE than algorithms based on Gaussian ML model (WF Gaussian and GS), when tested on simulated signals/images with different system matrices: random complex Gaussian matrix and discrete Fourier transform (DFT) matrix, for measurements having Poisson noise.

Furthermore, as expected the regularized algorithms designed for the Poisson model that exploit assumed properties of the true signals/images, such as sparsity of finite differences (anisotropic total variation) or of the coefficients of a discrete wavelet transform, can further lower the NRMSE compared to unregularized algorithms. Regarding the computational efficiency, in the unregularized case, the WF Poisson algorithm and GS decreased the NRMSE fastest but WF Poisson demonstrated higher reconstruction quality. In the regularized case, the regularized LSMM algorithm decreased the NRMSE with comparable speed performance as the unregularized algorithms, but with notably improved reconstruction accuracy (lower NRMSE).

In summary, the proposed algorithms are effective for both regularized and unregularized phase retrieval from Poisson measurements. Future work includes investigating Poisson plus Gaussian noise models, exploring why WF Gaussian fails under DFT matrix setting, establishing sufficient conditions for global convergence, investigating algorithms that can handle other kind of regularizers (e.g., ℓ_0 norm, deep learning methods), seeking for the optimal or even closer to optimal curvature, and testing algorithms derived for the Poisson noise model under a wider variety of experimental settings.

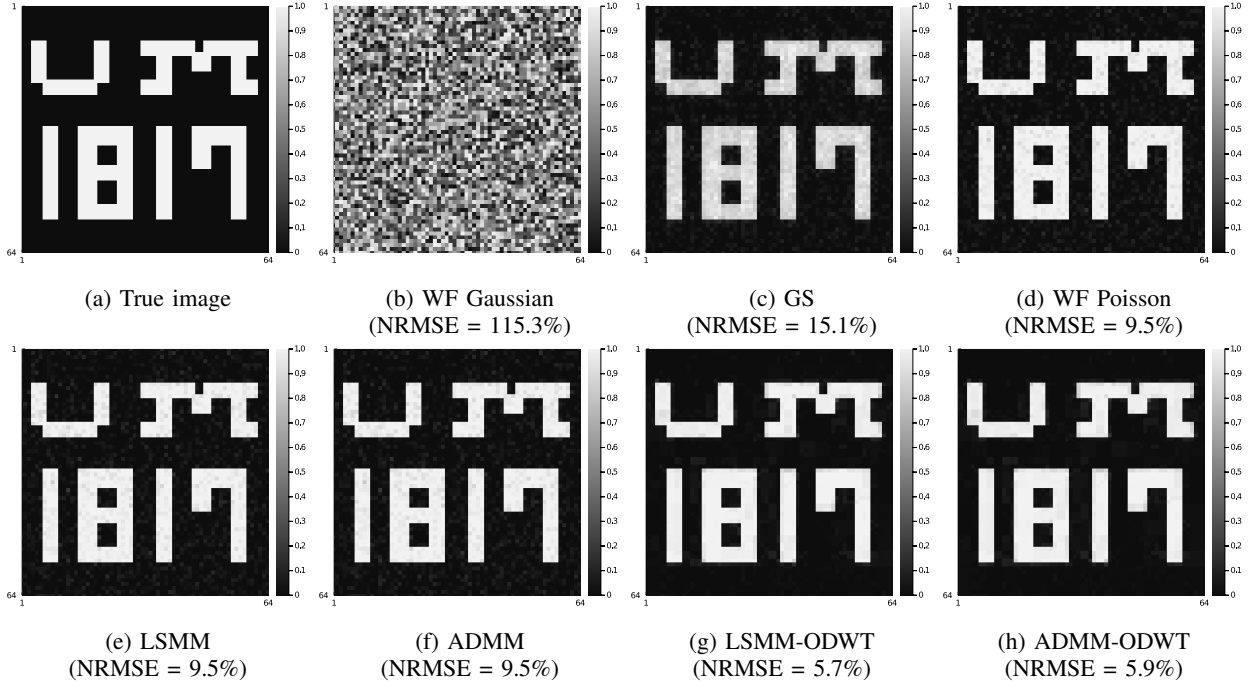


Fig. 5: Reconstructed image and corresponding NRMSE compared to the true image of size 64×64 , for a sensing system with $L = 21$ masked DFT matrices. The average of $|a'_i x|^2$ and b_i were set to 1 and 0.1, respectively.

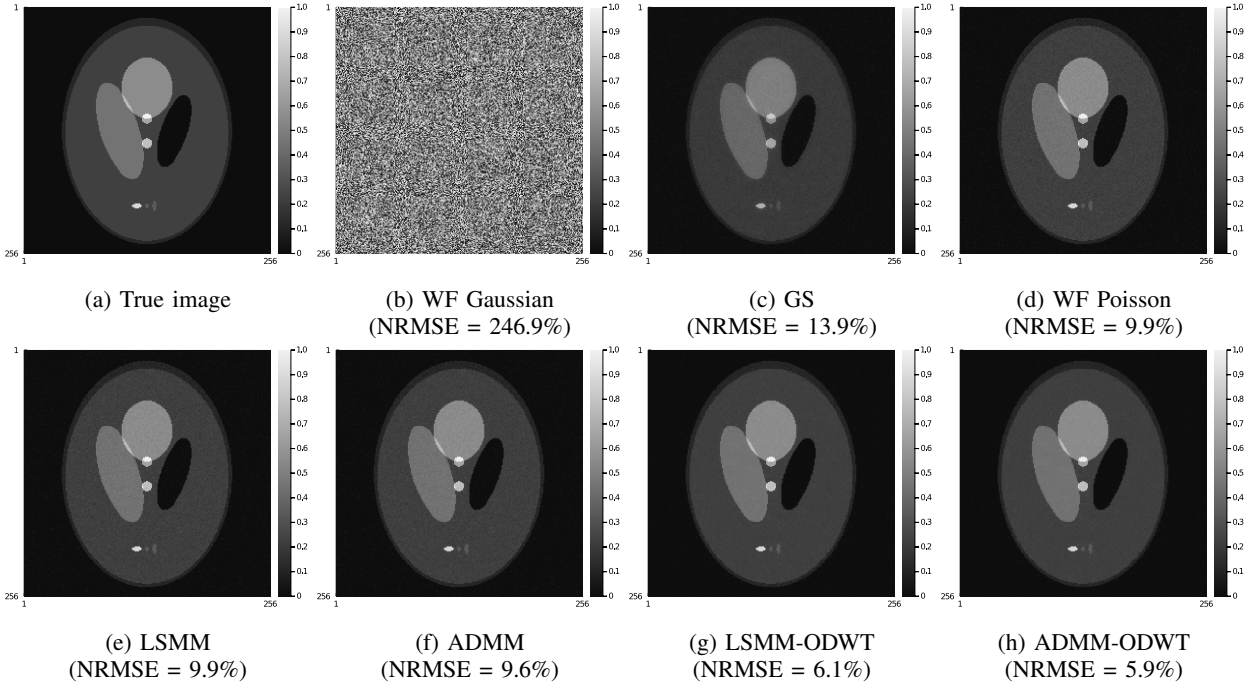


Fig. 6: Reconstructed image and corresponding NRMSE compared to the true image (Shepp-Logan phantom of size 256×256), for a sensing system with $L = 21$ masked DFT matrices. The average of $|a'_i x|^2$ and b_i were set to 1 and 0.1, respectively.

APPENDIX

This appendix proves that the curvature formula (19) provides a majorizer for the negative log-likelihood of the Poisson model that always is bounded above by the maximum curvature (7).

For Poisson phase retrieval, we drop the subscript i and irrelevant constants and focus on the negative log-likelihood for real case for simplicity:

$$h(r) = (r^2 + b) - y \log(r^2 + b), \quad (36)$$

where $r \in \mathbb{R}, y \geq 0, b \geq 0$.

One can generalize the majorizer derived here for (36) to the complex case by taking the magnitude and some other minor modifications.

First, we consider some simple cases:

- If $y = 0$, then (36) is a quadratic function, so no quadratic majorizer is needed.
- If $b = 0$ and $y > 0$ then (36) has unbounded 2nd derivative so no quadratic majorizer exists.
- If $b = 0$ and $r = 0$, then y must be zero because a Poisson random variable with zero mean can only take the value 0. Thus again quadratic majorizer is not needed.

So hereafter, we assume that $y > 0, b > 0$. Under these assumptions, the derivatives of (36) are:

$$\dot{h}(r) = 2r \left(1 - \frac{y}{r^2 + b} \right) \quad (37)$$

$$\ddot{h}(r) = 2 + 2y \frac{r^2 - b}{(r^2 + b)^2} \quad (38)$$

$$h^{(3)}(r) = \frac{2yr(3b - r^2)}{(r^2 + b)^3}, \quad (39)$$

where $h^{(3)}(r)$ denotes the third derivative. Clearly, $\dot{h}(r)$ is convex on $(-\infty, -\sqrt{3b}]$ and $[0, \sqrt{3b}]$, and concave on $[-\sqrt{3b}, 0]$ and $[\sqrt{3b}, +\infty)$, based on the sign of $h^{(3)}(r)$.

A quadratic majorizer of h at point s has the form:

$$H(r; s) = h(s) + \dot{h}(s)(r - s) + \frac{1}{2}c(s)(r - s)^2. \quad (40)$$

The derivative of this function (w.r.t. r) is:

$$\dot{H}(r; s) = c(s)(r - s) + \dot{h}(s). \quad (41)$$

By design, this kind of quadratic majorizer satisfies $H(s; s) = h(s)$ and $\dot{H}(s; s) = \dot{h}(s)$. From (39), we note that $r^2 = 3b$ is a maximizer of \dot{h} so the maximum

curvature is:

$$\ddot{h}(r) \leq 2y \frac{2b}{(4b)^2} + 2 = 2 + \frac{y}{4b}. \quad (42)$$

Proposition: $H(r; s)$ defined in (40) is a majorizer of $h(r)$ when $c(s) = c_{\text{imp}}(s)$, where:

$$c_{\text{imp}}(s) \triangleq \begin{cases} \ddot{h}(g(s)), & s \neq 0, \\ \lim_{s \rightarrow 0} \ddot{h}(g(s)), & s = 0, \end{cases} \quad (43)$$

where

$$g(s) \triangleq \frac{b + \sqrt{b^2 + bs^2}}{s}. \quad (44)$$

By construction, the proposed curvature $c(s)$ is at most the max curvature given in (42).

Proof: Because of the symmetry of $\ddot{h}(r)$, it suffices to prove the proposition for $s \geq 0$ without loss of generality. First we consider some trivial cases:

- 1) If $s = 0$, one can verify $\lim_{s \rightarrow 0} \ddot{h}(g(s)) = 2$. In this case, $H(r; s)$ is simply

$$\begin{aligned} H(r; 0) &= h(0) + \frac{1}{2}c(0)r^2 \\ &= r^2 + b - y \log(b) \\ &\geq r^2 + b - y \log(r^2 + b) = h(r). \end{aligned} \quad (45)$$

- 2) If $s = \sqrt{3b}$, one can verify

$$\ddot{h}(g(\sqrt{3b})) = 2 + \frac{y}{4b}. \quad (46)$$

So in this case $\ddot{h}(g(s))$ equals the maximum curvature.

Hereafter, we consider only $s > 0$ and $s \neq \sqrt{3b}$, so it suffices to prove that

$$\begin{aligned} \forall r \in (-\infty, s], \quad \dot{h}(r) &\geq \dot{H}(r; s), \\ \forall r \in [s, +\infty), \quad \dot{h}(r) &\leq \dot{H}(r; s), \end{aligned} \quad (47)$$

because if (47) holds, then $\forall \tilde{r} < s$:

$$\begin{aligned} H(s; s) - H(\tilde{r}; s) &= \int_{\tilde{r}}^s \dot{H}(r; s) dr \\ &\leq \int_{\tilde{r}}^s \dot{h}(r) dr = h(s) - h(\tilde{r}), \end{aligned} \quad (48)$$

and $\forall \tilde{r} > s$:

$$\begin{aligned} H(\tilde{r}; s) - H(s; s) &= \int_s^{\tilde{r}} \dot{H}(r; s) dr \\ &\geq \int_s^{\tilde{r}} \dot{h}(r) dr = h(\tilde{r}) - h(s). \end{aligned} \quad (49)$$

Together with $H(s; s) = h(s)$, we will have shown $H(r; s) \geq h(r), \forall r \in \mathbb{R}$ after showing (47).

Substituting $\dot{H}(r; s) = c(s)(r - s) + \dot{h}(s)$, one can verify that showing (47) simplifies to showing

$$c_{\text{imp}}(s) \geq \frac{\dot{h}(r) - \dot{h}(s)}{r - s}, \quad \forall r \in \mathbb{R}, r \neq s. \quad (50)$$

Furthermore, when $s > 0$, the parabola $H(\cdot; s)$ is symmetric about its minimizer:

$$\begin{aligned} a = a(s) &\triangleq \operatorname{argmin}_r H(r; s) = s - \frac{\dot{h}(s)}{c_{\text{imp}}(s)} \\ &= \frac{s\ddot{h}(g(s)) - \dot{h}(s)}{\ddot{h}(g(s))} \geq 0. \end{aligned} \quad (51)$$

This minimizer is nonnegative because $\dot{h}(s) \leq 2s$ and

$$\begin{aligned} c_{\text{imp}}(s) = \ddot{h}(g(s)) &= 2 + \frac{ys^2(b + \sqrt{b^2 + bs^2})}{b(b + s^2 + \sqrt{b^2 + bs^2})^2} \\ &\geq 2. \end{aligned} \quad (52)$$

Thus, if $h(r) \leq H(r; s)$ when $r \geq 0$, we have $h(-r) = h(r) \leq H(r; s) \leq H(-r; s) = H(r + 2a; s)$, so it suffices to prove (50) only for $r \geq 0$, which simplifies (50) to showing

$$c_{\text{imp}}(s) \geq \frac{\dot{h}(r) - \dot{h}(s)}{r - s}, \quad \forall r \geq 0, r \neq s. \quad (53)$$

In short, if (53) holds, then $H(r; s) \geq h(r)$, $\forall r \in \mathbb{R}$.

To prove (53), we first exploit a useful property of $c_{\text{imp}}(s)$. The intuition behind $c_{\text{imp}}(s)$ is that the affine function connecting points $(g(s), \dot{h}(g(s)))$ and $(s, \dot{h}(s))$ is tangent to $\dot{h}(r)$ at point $r = g(s)$, so that one can verify

$$\ddot{h}(g(s)) = c_{\text{imp}}(s) = \frac{\dot{h}(g(s)) - \dot{h}(s)}{g(s) - s}, \quad g(s) \neq s. \quad (54)$$

Moreover, one can verify $g(s) = s$ implies $s = \sqrt{3b}$ for $s > 0$, so (54) is valid by our assumption above ($s > 0$ and $s \neq \sqrt{3b}$). Let $f(r) = (\dot{h}(r) - \dot{h}(s))/(r - s)$, where $r \geq 0$ and $r \neq s$, plugging in $\dot{h}(r)$ and $\dot{h}(s)$ yields:

$$f(r) = 2 + \frac{2y(sr - b)}{(s^2 + b)(r^2 + b)}. \quad (55)$$

Differentiating w.r.t. r leads to:

$$\dot{f}(r) = \frac{2y}{s^2 + b} \cdot \frac{-sr^2 + 2br + bs}{(r^2 + b)^2}, \quad (56)$$

where one can verify the positive root of $-sr^2 + 2br + bs = 0$ is $g(s)$. Together with $\dot{f}(r) > 0$ when $r \in (0, g(s))$ and $\dot{f}(r) < 0$ when $r \in (g(s), \infty)$, we have that (53) holds because $f(r)$ achieves its maximum at $f(g(s))$:

$$f(r) \leq f(g(s)) = c_{\text{imp}}(s). \quad \blacksquare \quad (57)$$

REFERENCES

- [1] K. Jaganathan, Y. C. Eldar, and B. Hassibi. *Phase retrieval: an overview of recent developments*. 2015.
- [2] P. Grohs, S. Koppensteiner, and M. Rathmair. “Phase retrieval: uniqueness and stability”. In: *SIAM Review* 62.2 (2020), 301–50.
- [3] P. Jaming. “Phase retrieval techniques for radar ambiguity problems.” In: *J. Four. Anal. Appl.* 5.4 (1999), pp. 309–329.
- [4] R. P. Millane. “Phase retrieval in crystallography and optics”. In: *J. Opt. Soc. Am. A* 7.3 (Mar. 1990), 394–411.
- [5] J. Dainty and J. Fienup. “Phase retrieval and image reconstruction for astronomy”. In: *Imag. Recov. Theory Appl.* 13 (Jan. 1987), pp. 231–275.
- [6] L. R. Rabiner and B.-H. Juang. *Fundamentals of Speech Recognition*. Eng. Clif., NJ: Pren. Hall, 1993.
- [7] T. Qiu, P. Babu, and D. P. Palomar. “PRIME: phase retrieval via majorization-minimization”. In: *IEEE Trans. Sig. Proc.* 64.19 (Oct. 2016), 5174–86.
- [8] E. Candes, X. Li, and M. Soltanolkotabi. “Phase Retrieval via Wirtinger Flow: Theory and Algorithms”. In: *IEEE Trans. Info. Theory* 61.4 (Apr. 2015), pp. 1985–2007.
- [9] R. W. Gerchberg and W. O. Saxton. “Practical Algorithm for Determination of Phase from Image and Diffraction Plane Pictures”. In: *OPTIK* 35.2 (1972), 237–246.
- [10] P. Thibault and M. Guizar-Sicairos. “Maximum-likelihood refinement for coherent diffractive imaging”. In: *New J. of Phys.* 14.6 (June 2012), p. 063004.
- [11] L. Bian, J. Suo, J. Chung, X. Ou, C. Yang, F. Chen, and Q. Dai. “Fourier ptychographic reconstruction using Poisson maximum likelihood and truncated Wirtinger gradient”. In: *Nature Sci. Rep.* 6.1 (2016).
- [12] A. Goy, K. Arthur, S. Li, and G. Barbastathis. “Low photon count phase retrieval using deep learning”. In: *Phys. Rev. Lett.* 121.24 (Dec. 2018), p. 243902.
- [13] R. Xu, M. Soltanolkotabi, J. P. Haldar, W. Unglaub, J. Zusman, A. F. J. Levi, and R. M. Leahy. *Accelerated Wirtinger Flow: A fast algorithm for ptychography*. 2018.
- [14] D. A. Barmherzig and J. Sun. “Low-photon holographic phase retrieval”. In: *OSA: Computational Optical Sensing and Imaging*. 2020.
- [15] I. Vazquez, I. E. Harmon, J. C. R. Luna, and M. Das. “Quantitative phase retrieval with low

- photon counts using an energy resolving quantum detector". In: *J. Opt. Soc. Am. A* 38.1 (Jan. 2021), 71–9.
- [16] H. Lawrence, D. A. Barmherzig, H. Li, M. Eickenberg, and M. Gabriele. *Phase retrieval with holography and untrained priors: Tackling the challenges of low-photon nanoscale imaging*. 2020.
 - [17] D. L. Snyder, C. W. Helstrom, A. D. Lanterman, M. Faisal, and R. L. White. "Compensation for readout noise in CCD images". In: *J. Opt. Soc. Am. A* 12.2 (Feb. 1995), 272–83.
 - [18] K. Choi and A. D. Lanterman. "Phase retrieval from noisy data based on minimization of penalized I-divergence". In: *J. Opt. Soc. Am. A* 24.1 (Jan. 2007), 34–49.
 - [19] E. J. Candes, Y. C. Eldar, T. Strohmer, and V. Voroninski. "Phase retrieval via matrix completion". In: *SIAM J. Imaging Sci.* 6.1 (2013), 199–225.
 - [20] Y. Chen and E. J. Candes. "Solving random quadratic systems of equations is nearly as easy as solving linear systems". In: *Comm. Pure Appl. Math.* 70.5 (May 2017), 822–83.
 - [21] H. Chang and S. Marchesini. "Denoising Poisson phaseless measurements via orthogonal dictionary learning". In: *Optics Express* 26.16 (Aug. 2018), 19773–96.
 - [22] Y. Zhang, P. Song, and Q. Dai. "Fourier ptychographic microscopy using a generalized Anscombe transform approximation of the mixed Poisson-Gaussian likelihood". In: *Optics Express* 25.1 (Jan. 2017), 168–79.
 - [23] I. Kang, F. Zhang, and G. Barbastathis. "Phase extraction neural network (PhENN) with coherent modulation imaging (CMI) for phase retrieval at low photon counts". In: *Optics Express* 28.15 (July 2020), 21578–600.
 - [24] D. L. Snyder, A. M. Hammoud, and R. L. White. "Image recovery from data acquired with a charge-coupled-device camera". In: *J. Opt. Soc. Am. A* 10.5 (May 1993), 1014–23.
 - [25] M. Makitalo and A. Foi. "Optimal Inversion of the Generalized Anscombe Transformation for Poisson-Gaussian Noise". In: *IEEE Transactions on Image Processing* 22.1 (2013), pp. 91–103.
 - [26] H. Zhang and D. P. Mandic. "Is a complex-valued stepsize advantageous in complex-valued gradient learning algorithms?" In: *IEEE Trans. Neural Net. Learn. Sys.* 27.12 (Dec. 2016), 2730–5.
 - [27] D. Böhning and B. G. Lindsay. "Monotonicity of quadratic approximation algorithms". In: *Ann. Inst. Stat. Math.* 40.4 (Dec. 1988), 641–63.
 - [28] H. Chang, Y. Lou, Y. Duan, and S. Marchesini. "Total variation-based phase retrieval for poisson noise removal". In: *SIAM journal on imaging sciences* 11.1 (2018), pp. 24–55.
 - [29] T. Qiu and D. P. Palomar. "Undersampled sparse phase retrieval via majorization-minimization". In: *IEEE Trans. Sig. Proc.* 65.22 (Nov. 2017), 5957–69.
 - [30] H. Zhang, Y. Liang, and Y. Chi. "A nonconvex approach for phase retrieval: Reshaped Wirtinger flow and incremental algorithms". In: *J. Mach. Learning Res.* 18.141 (2017), 1–35.
 - [31] K. Lange. "A gradient algorithm locally equivalent to the EM Algorithm". In: *J. Royal Stat. Soc. Ser. B* 57.2 (1995), 425–37.
 - [32] D. R. Hunter and K. Lange. "A tutorial on MM algorithms". In: *American Statistician* 58.1 (Feb. 2004), 30–7.
 - [33] J. de Leeuw and K. Lange. "Sharp quadratic majorization in one dimension". In: *Comp. Stat. Data Anal.* 53.7 (May 2009), 2471–84.
 - [34] I. Daubechies, M. Defrise, and C. De Mol. "An iterative thresholding algorithm for linear inverse problems with a sparsity constraint". In: *Comm. Pure Appl. Math.* 57.11 (Nov. 2004), 1413–57.
 - [35] A. Beck and M. Teboulle. "A fast iterative shrinkage-thresholding algorithm for linear inverse problems". In: *SIAM J. Imaging Sci.* 2.1 (2009), 183–202.
 - [36] D. Kim and J. A. Fessler. "Adaptive restart of the optimized gradient method for convex optimization". In: *J. Optim. Theory Appl.* 178.1 (July 2018), 240–63.
 - [37] S. Boyd, N. Parikh, E. Chu, B. Peleato, and J. Eckstein. "Distributed Optimization and Statistical Learning via the Alternating Direction Method of Multipliers". In: *Found. Trends Mach. Learn.* 3.1 (Jan. 2011), pp. 1–122.
 - [38] Y. Wang, W. Yin, and J. Zeng. "Global convergence of ADMM in nonconvex nonsmooth optimization". In: *J. Sci. Comp.* 78.1 (2019), 29–63.
 - [39] Y. Shechtman, Y. C. Eldar, O. Cohen, H. N. Chapman, J. Miao, and M. Segev. "Phase Retrieval with Application to Optical Imaging: A contemporary overview". In: *IEEE Sig. Proc. Mag.* 32.3 (2015), pp. 87–109.
 - [40] T. Bendory, R. Beinert, and Y. C. Eldar. "Fourier Phase Retrieval: Uniqueness and Algorithms". In: *Compressed Sensing and its Applications*. Applied and Numerical Harmonic Analysis. Springer Intl. Publishing, 2018, pp. 55–91.